Operando monitoring of state of health forlithium battery via fiber optic ultrasoundimaging system

Geng Chen, Anqi Wang, Yi Zhang, Fujun Zhang, Dongchen Xu,Yueqi Liu, Zhi Zhang, Zhijun Yan, Zhen Li, Hao Li* and Qizhen Sun*

Operando monitoring of state of health for lithium battery via fiber optic ultrasound imaging system

Geng Chen, Anqi Wang, Yi Zhang, Fujun Zhang, Dongchen Xu, Yueqi Liu, Zhi Zhang, Zhijun Yan, Zhen Li, Hao Li and Qizhen Sun

---

Related articles

Highly sensitive microfiber ultrasound sensor for photoacoustic imaging

Perry Ping Shum, Gerd Keiser, Georges Humbert, Dora Juan Juan Hu, A. Ping Zhang, Lei Su

Opto-Electronic Advances   2023   **6**, 230065   doi: 10.29026/oea.2023.230065

Optical micro/nanofiber enabled tactile sensors and soft actuators: A review

Lei Zhang, Yuqi Zhen, Limin Tong

Opto-Electronic Science   2024   **3**, 240005   doi: 10.29026/oes.2024.240005

Specialty optical fibers for advanced sensing applications

Huanhuan Liu, Dora Juan Juan Hu, Qizhen Sun, Lei Wei, Kaiwei Li, Changrui Liao, Bozhe Li, Cong Zhao, Xinyong Dong, Yuhan Tang, Yihong Xiao, Gerd Keiser, Perry Ping Shum

Opto-Electronic Science   2023   **2**, 220025   doi: 10.29026/oes.2023.220025

Adaptive decentralized AI scheme for signal recognition of distributed sensor systems

Shixiong Zhang, Hao Li, Cunzheng Fan, Zhichao Zeng, Chao Xiong, Jie Wu, Zhijun Yan, Deming Liu, Qizhen Sun

Opto-Electronic Advances   2024   **7**, 240119   doi: 10.29026/oea.2024.240119

Operando monitoring of state of health for lithium battery via fiber optic ultrasound imaging system

Geng Chen[1], Anqi Wang[1], Yi Zhang[2], Fujun Zhang[1], Dongchen Xu[1], Yueqi Liu[1], Zhi Zhang[1], Zhijun Yan[1,3], Zhen Li[2], Hao Li[1]* and Qizhen Sun[1,3]*

With the rapid development of lithium batteries, it's of great significance to ensure the safe use of it. An ultrasound imaging system based on fiber optic ultrasound sensor has been developed to monitor the internal changes of lithium batteries. Based on Fabry-Perot interferometer (FPI) structure which is made of a glass plate and an optical fiber pigtail, the ultrasound imaging system possesses a high sensitivity of 558 mV/kPa at 500 kHz with the noise equivalent pressure (NEP) of only 63.5 mPa. For the frequency response, the ultrasound sensitivity is higher than 13.1 mV/kPa within the frequency range from 50 kHz to 1 MHz. Meanwhile, the battery imaging system based on the proposed sensor has a superior resolution as high as 0.5 mm. The performance of battery safety monitoring is verified, in which three commercial lithium-ion ferrous phosphate/graphite (LFP||Gr) batteries are imaged and the state of health (SOH) for different batteries is obtained. Besides, the wetting process of an anode-free lithium metal batteries (AFLMB) is clearly observed via the proposed system, in which the formation process of the pouch cell is analyzed and the gas-related "unwetting" condition is discovered, representing a significant advancement in battery health monitoring field. In the future, the commercial usage can be realized when sensor array and artificial intelligence technology are adopted.

Keywords: fiber optic ultrasound sensor; Fabry-Perot interferometer; battery health monitoring; formation process

Introduction

Lithium batteries, with their high energy storage density and high durability, are extensively used as the power source of many electronic products[1]. Nowadays, with the rapid development of electric vehicles, producers tend to fabricate the batteries with higher energy density and smaller size. Among them, the anode of the anode-free lithium metal batteries (AFLMB) is lithium metal instead of traditional graphite, which upgrades its capacity and energy density[2–4]. Nevertheless, the performance improvement is accompanied by potential danger[5]. Under the irregular use such as manufacturing issues, physical damage, electrical abuse and so on, lithium batteries are prone to suffer from capacity decay, lithium plating, gas

generation and even explosion[6]. Therefore, it's of great significance to ensure the safety in utilizing lithium batteries.

Recently, many methods have been applied to battery health monitoring (BHM) field. Apart from disassembling faulty batteries to check the defects, researchers have invented some in-operando monitoring methods by adopting electron[7], X-ray[8,9], and neutron diffraction[10,11], to acquire the SOH for the pouch cells, but these manners suffer from deficient penetration depth, insensitivity to gas, high cost and being harmful to human body. They have also found that the voltage relaxation phenomenon during cycling[12] and asymmetries between the average voltages of charging and discharging process[13] may demonstrate great possibility of lithium deposition on the anode, but this method is not very intuitive. Besides, utilizing thermal imaging to investigate the inner change of lithium-ion batteries during the charging process is also carried out[14], but the insufficient resolution limits its further application. In addition to the traditional means talked above, optical detection methods are also widely used in BHM. The fiber Bragg grating (FBG) sensors with the advantage of great stability[15,16] are utilized to simultaneously decode the inner temperature and surface strain of the battery, which prevent the battery from disastrous thermal events and gas-release events[17−20]. And the tilted fiber Bragg grating (TFBG) sensors with the surface plasmon resonance effect are also used to observe the ions activities[21]. But the FBG sensors must be attached or inserted to the battery to acquire the variation of strain and temperature, which makes it less competitive in the commercial field. In the meantime, the virtual sensor based on particle filter is utilized for estimating the state of charge (SOC) and internal temperature of lithium-ion batteries[22], which shows a new approach in combining BHM with machine learning technology[23]. Generally speaking, the methods mentioned above has the limitation of lack for intuitiveness, low resolution and insufficient information.

Due to the advantages of high-penetration-depth, noncontact, and high sensitivity to the interface between electrolyte/electrodes and gas, the ultrasound technology is quite applicable in the BHM area. Some researchers have adopted ultrasound method in fixed-point[24−26] and scanning tests[27], which demonstrate the feasibility of this manner in BHM. However, traditional electronic ultrasound equipment such as the piezoelectric transducer (PZT), will be greatly disturbed by electromagnetic interference (EMI), failing to work under those extreme environments, such as electricity substation. Besides, the electronic hydrophone possesses a poor sensitivity of about several tens of millivolts per megapascal and a large size of several centimeters, which makes it hard to form an array to realize fast-scanning.

Fiber optic sensors, with unique advantages of small size, high sensitivity and immunity to EMI, are very suitable to the ultrasound detection[28−30]. Sensors based on phase modulation with higher sensitivity are widely used[31], including Sagnac, Mach-Zehnder (MZ), Michelson and Fabry-Perot (FP) interferometers[32−36]. Among these, diaphragm-based extrinsic FP interferometric ultrasound sensors have the advantages of compactness and ultra-high sensitivity[37−39]. In addition, the frequency response of the fiber optic extrinsic FP interferometric sensors can be altered by changing the structure parameters and material of the diaphragm[40]. With the advantage of high sensitivity and stablitily[41,42], the sensor can pick up the low-intensity ultrasound signal among the noise to acquire the battery state more precisely. And the miniaturization enables the sensor to integrate with high resolution. Consequently, fiber optic ultrasound sensors based on FP interferometer have great potential in the field of BHM.

In this paper, a fiber optic ultrasound imaging system based on FP interferometric sensor has been proposed and demonstrated. And to our knowledge, this is the first time to realize the visualization of batteries by adopting fiber optic FPI ultrasound sensor. With the help of Q point self-correction technology, high sensitivity and low NEP have been demonstrated. The high performance of the sensor enables the imaging system to reach a sufficient resolution in battery health monitoring. Besides, the gas generation phenomenon of several commercial LFP||Gr batteries has been successfully discovered. The electrolyte infiltration process and the first cycle (i.e., formation) process of an AFLMB have been observed, indicating the significant application prospects of the imaging system.

Methods

Fiber optic ultrasound sensor

In order to satisfy the needs for lithium battery monitoring, it is of great importance to detect with high sensitivity and compactness. An acoustic sensor based on Fabry-Perot interferometer is proposed to perform acoustic

detection. The schematic diagram and photograph of the proposed sensor tip are presented in Fig. 1(a) and 1(b), respectively. The sensor tip is composed of a glass plate which is sensitive to the acoustic pressure, a glass capillary, a ceramic ferrule, and the single mode fiber (SMF). The glass plate and the glass capillary are glued by UV-curable adhesive. The distance between the glass plate and the SMF end face is precisely controlled by a translation stage. Then, the adhesive is applied to the ferrule and the sensor structure can be fixed under UV light. As two reflective mirrors of the fiber FPI, the glass plate and the facet of the SMF are coated with silver by vacuum evaporation to enhance their reflectivity, and the thickness is 100 nm and 10 nm, resulting in a reflectivity of around 99% and 50%, respectively. As shown in Fig. 1(b), the sensor tip is about 4.5 mm in diameter, which is suitable to construct the high-resolution battery imaging system with the miniaturization.

When the ultrasound wave is imposed on the sensor tip, the front glass plate of the sensor will vibrate accordingly, leading to the distance change between the plate and fiber facet. The sensitivity of the plate vibration can be written as

$$S = \frac{\Delta L}{\Delta P} = \frac{3(1 - v^2) \cdot D^4}{256 E t^3} , \qquad (1)$$

where $v = 0.22$ and $E = 70$ GPa are the Poisson ratio and the Young's modulus of the glass plate, respectively. ΔL and ΔP are the vibration amplitude of the plate and imposed ultrasound pressure. D and t are the diameter and thickness of the glass plate, respectively. Due to the linear characteristic of the devices, the sensitivity of the sensor can be regarded as the sensitivity of the plate vibration ΔL, which is proportional to the fourth power of the diameter and inversely proportional to the third power of the thickness. Therefore, although the size of the sensor is larger than the sensor based on the fiber tip, the

sensitivity of the structure is much higher.

As a FPI based structure, the reflected beam from the sensor is a result of the multi-beam interference. The change of cavity length in Eq. (1) will further influence the optical pace difference (OPD), resulting in the reflectivity variation of the FPI. When an interrogation light is pumped into the SMF, the intensity change of the reflected beam indicates the arrival of the ultrasound wave. In the conversion of the vibration amplitude to the laser intensity variation, the derivation of the spectrum is essential. To acquire a high sensitivity, the spectrum should possess a high fineness:

$$S = \frac{\pi \sqrt{R}}{1 - R} , \qquad (2)$$

where R is the reflectivity of the reflective mirrors in the FPI. So as to improve the spectrum fineness, the reflectivity of the two mirrors must be high enough. The reflected spectrum of the fabricated sensor is presented in Fig. 1(c), in which the free spectrum range (FSR) is about 22.3 nm with a full width at half magnitude (FWHM) of 3.74 nm, so the fineness is calculated to be 5.96. To achieve the optimum sensitivity, the wavelength of the interrogation laser should be set to the maximum slope of the interferometer transfer function (ITF). The derivation of the reflected spectrum is also illustrated in Fig. 1(c), which shows a maximum value of -0.2 nm^{-1} when the wavelength is 1551.1 nm. Therefore, the wavelength of the interrogation laser is set as 1551.1 nm to attain the optimum performance of the sensor.

Besides, the ultrasound frequency we used for battery detection also need further analysis. As a membrane-vibrating based ultrasound probe, the central frequency of the probe can be written as

$$f_{00} = \frac{10.21t}{\pi D^2} \sqrt{\frac{E}{3\rho(1 - v^2)}} , \qquad (3)$$
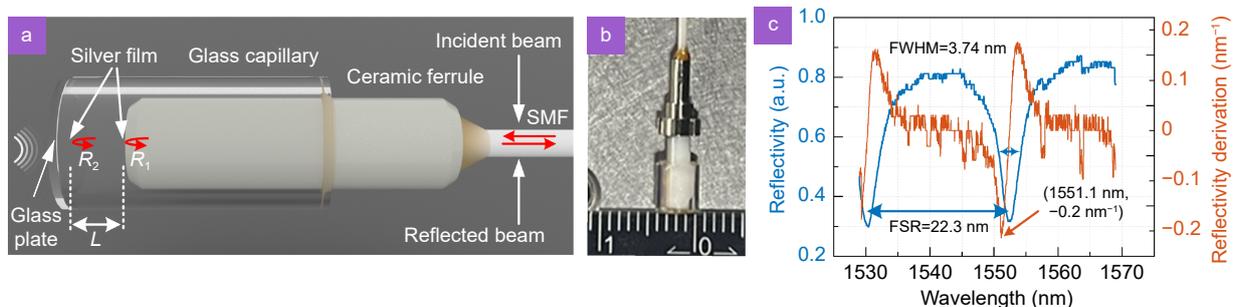

Fig. 1 | (**a**) Schematic of the fiber optic FPI ultrasound sensor tip. (**b**) Photograph of the sensor tip. (**c**) The reflected spectrum and its derivation of the fiber optic FP ultrasound sensor.

where $\rho = 2.5 \times 10^3$ kg/m³ is the density of the membrane material. According to the Eq. (3), the resonant frequency is proportional to the thickness of the plate and inversely proportional to the square of the diameter. Since the pouch cell with aluminum laminated film package will block the high frequency ultrasound waves, the resonant frequency of the membrane should satisfy both enough penetrability and appropriate imaging resolution. Hence, the membrane is a glass plate with 2.5 mm in diameter and 0.5 mm in thickness, which results in a resonant frequency of below 1 MHz. As a resonant structure, the sensitivity becomes the highest when the frequency is around the resonant frequency. While the flat response occurs when the frequency is higher than the resonant frequency.

Demodulation system setup for ultrasound sensor

To obtain the high-precision ultrasound waves, the demodulation system based on a tunable laser is set up, whose system configuration is illustrated in Fig. 2(a). The interrogation light emitted from the tunable laser (Santec, TSL-710, the linewidth is 100 kHz) will enter the sensor through the circulator, and be reflected by the sensor tip into the circulator. Then the photodetector (PD, Guangshi, the bandwidth is 100 MHz) receives the reflected beam and converts it into electrical signal, in which the direct current (DC) component is received by the DAQ 2 (USB-6002, NI) and analyzed on the PC, while the alternative current (AC) component is received by the DAQ 1 (PCIE 8586) and output as the ultrasound signal. When the ultrasound wave is applied to the sensor, the intensity of the reflected beam fluctuates accordingly.

In order to obtain the optimum sensitivity, the Q point self-correction method has been proposed. Before detecting the ultrasound, the tunable laser will change its wavelength from 1530 nm to 1570 nm with an interval of 0.002 nm. The DC components at different wavelength is stored and plotted, which forms the reflected spectrum. In our experiment, the reflected spectrum will have slightly drift, while the shape and intensity of it won't easily change. Therefore, we calculate the derivation of the reflected spectrum, find out the maximum slope of it and record the amplitude of the DC component as Q point. In the meantime, whether the slope is positive or negative is also found out.

When the amplitude of the DC component is changing, the system will analyze the situation and change the wavelength of the tunable laser to make the DC component stabilized at Q point. In this way, the ultrasound sensing system can continually acquire the optimum sensitivity along with the imaging process. In the meantime, the medium that we used in the battery test is silicone oil, which is quite suitable to keep the spectrum stable and unchanged. The stability of the sensor by using this interrogation system is further demonstrated in Fig. S2.

Frequency response and noise equivalent pressure

To calibrate the detecting performance of this sensor, a water immersed PZT (Olympus, V318) is used in the experiment. The sensor is placed 30 mm away against the PZT, as shown in Fig. S1(a) and S1(b). The PZT is driv-
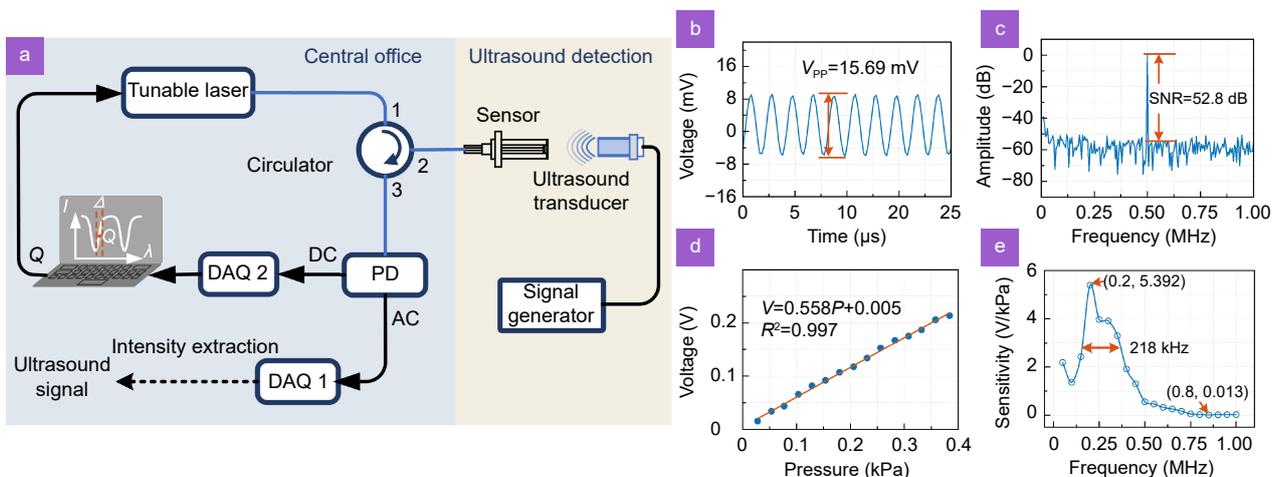

Fig. 2 | (a) The schematic diagram of the ultrasound sensing demodulation system. Detected signals when the voltage frequency is 500 kHz in (b) time domain and (c) frequency domain. (d) The output voltages of the sensor when ultrasound with different pressure is applied. (e) The frequency response of the sensor.

en by a sinusoidal voltage signal generator (RIGOL, DG1032z). The signal in Fig. 2(b) is detected by the sensor when the ultrasound frequency is 500 kHz. The amplitude of the signal is 15.69 mV, and it has a smooth curve and low noise without filtering operation. As presented in Fig. 2(c) and Fig. S1(c), since the signal-to-noise ratio (SNR) is 52.8 dB and the ultrasound pressure applied to the sensor is 27.73 Pa, the NEP is calculated to be 63.5 mPa at 500 kHz. Compared with conventional PZT, the sensor has an excellent performance in ultrasound detection, which can be seen in Table S1. The low NEP of around 63.5 mPa enables the system to detect ultrasound signals with low noise and high SNR.

We further utilize the generator to simulate the PZT which produces ultrasound waves at 500 kHz with different pressure. The amplitude of the excitation voltages can change from 1 V to 15 V with an interval of 1 V, and at each amplitude level, a commercial hydrophone (Precision Acoustics, ML4X50) is used to calibrate the ultrasound pressure emitted by the PZT. As illustrated in Fig. 2(d), the sensor response has a good linearity with a high sensitivity of about 558 mV/kPa. Besides, the sensor's frequency response is calibrated by measuring the sensitivity at different frequency. The measuring frequency range is set below 1 MHz with a step length of 50 kHz, and the system sampling rate is 5 MHz. As demonstrated in Fig. 2(e), the sensor possesses a relatively high sensitivity at around 200 kHz, and the sensitivity is larger

than 13.1 mV/kPa within the measured frequency range from 50 kHz to 1 MHz. With the low resonant frequency and high spectrum fineness, the sensor possesses a high sensitivity in the bandwidth, which makes it greatly competitive in BHM field.

Results and discussion

Fixed-point ultrasound monitoring of the battery

In order to test the feasibility of the sensor for BHM, a fixed-point ultrasound detection test on three LFP‖Gr batteries is carried out. The batteries are respectively labeled with faulty battery, circulated battery and healthy battery according to their charging-discharging performance. As described in Fig. 3(a), the batteries are placed between the sensor and the PZT. The ultrasound wave emitted by the PZT ultrasound transducer will pass through the battery and be received by the sensor. The time of flight (ToF) in the experiment can be calculated as follows:

$$ToF = \frac{L_{\text{oil}}}{v_{\text{oil}}} + \frac{L_{\text{battery}}}{v_{\text{battery}}} \ , \tag{4}$$

where L_{oil} and L_{battery} is the length of the ultrasound transmitting in silicone oil and battery, respectively. And v_{oil} and v_{battery} are respectively the average speed of the ultrasound transmitting in silicone oil and battery. Hence, the average speed of the ultrasound transmitting in the battery is the key factor that results in the great difference of ToF between the healthy and faulty battery.
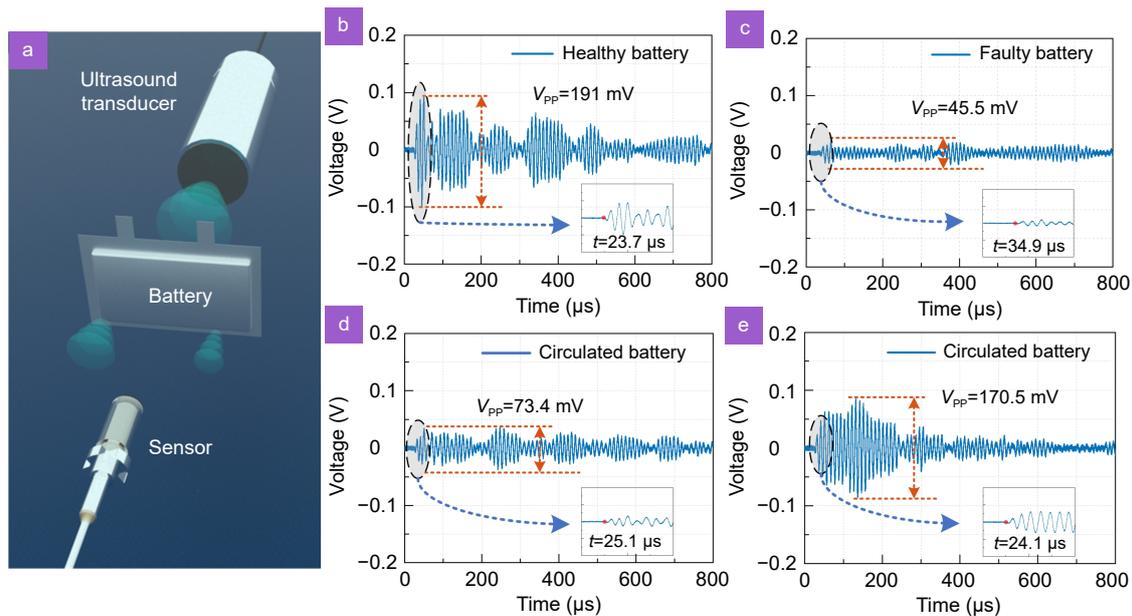

Fig. 3 | (a) The simplified experiment setup of the fixed-point detection. Signals from the LFP‖Gr batteries which are **(b)** healthy and **(c)** faulty. **(d, e)** Signals from different parts of the battery which cycles for 2000 times, respectively.

Since the speed of ultrasound in gas is far slower than it in the oil and battery, the ToF for faulty battery is much longer than the ToF in the healthy battery.

As illustrated in Fig. 3(b–e), the signal of healthy battery possesses a higher intensity and shorter ToF compared with the other two batteries. The faulty battery, which cannot be charged or discharged anymore, has the smallest intensity and longest ToF. The signals in Fig. 3(d) and 3(e) are from the same battery, while their intensity and ToF are quite different, which indicates that this battery is deteriorating and a small amount of gas generates while some part of the battery remain "wetted".

When undesired side reactions happen, the gas generates accordingly and the battery fails. The incident ultrasound can be greatly reflected by the electrodes/electrolyte-gas interface and slowed down. Therefore, the signal from the flaw area appears to be low-intensity and long-time-of-flight compared to that from the normal part. Hence, the signal from the healthy battery in Fig. 3(b) indicates that it has a good SOH, while the faulty battery has a terrible SOH. SOH of the battery cycled for 2000 times is not well but it's better than the faulty one. In summary, the results of the ultrasound test are highly consistent with their charging and discharging performance. Therefore, the fixed-point ultrasound detection can prejudge the SOH of battery, providing information for further failure recognition.

The imaging resolution of the BHM system

The BHM system setup is described in Fig. 4(a). the translation stage can move the fiber optic probe and PZT together in *x*- and *z*- direction, realizing the multipoint detection of the object. To acquire the ultrasound image, the peak-to-peak values of every ultrasound signal in the imaging region is collected and normalized. The normalized values are converted to color scale and the ultrasound transmission image can be formed.

To simulate the condition that may happen in the batteries, a 5 mm thick acrylic plate is manufactured with four air slits, which is shown in Fig. 4(b). The air slits have the width of 3 mm, 2 mm, 1 mm and 0.5 mm, respectively. In Fig. 4(c), the green parts in the middle of the picture represent the four air slits, indicating that the air slits can be clearly detected and distinguished. Therefore, the resolution of the system is less than 0.5 mm, which is appropriate for BHM. The blue parts are the imaging result of two grippers that can almost block the transmission of the ultrasound wave. The green parts on the edge of the acrylic plate are caused by the acoustic impedance mismatch between the plate and water.

Commercial battery testing

Furthermore, the LFP||Gr batteries with different cycling conditions are imaged through this BHM system. As shown in Fig. 5(a), the LFP||Gr battery has a size of 76 mm×47 mm×5.6 mm and the scanning time is about 50 min, which can be further improved by using fiber optic ultrasound sensor array. The edge of the battery has a small ultrasound transmission while the majority of the central part is green which is illustrated in Fig. 5(b),
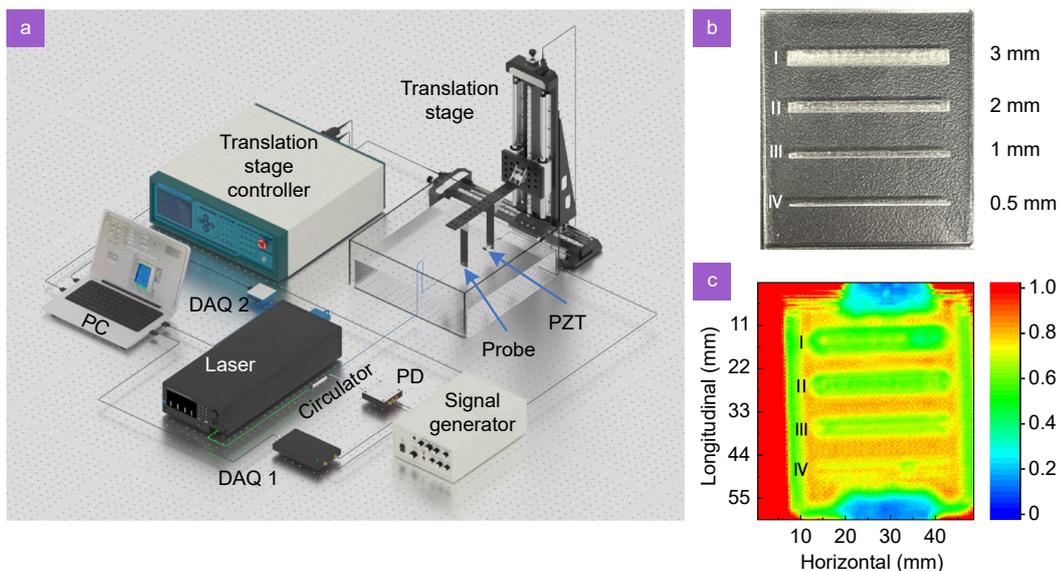

Fig. 4 | (a) The schematic diagram of the fiber optic ultrasound BHM system setup. **(b)** The photograph of the acrylic plate. **(c)** The imaging result of the acrylic plate.

indicating a higher ultrasound transmission. The blue edge area in the imaging result of the battery cycling for 2000 times is larger than that of the healthy battery, and the low-transmission part even exists in the middle of the battery, as described in Fig. 5(c). What's worse is that it's almost entirely blue in Fig. 5(d). The green part on the outermost region is the package of the battery, which can be seen in the three figures discussed above. The unhealthy battery can be determined by comparing the transmission of ultrasound at the inner part with that at the edge area.

The signal in Fig. 5(b) indicates that the healthy battery which is newly injected with electrolyte exhibits a good SOH, while the faulty one in Fig. 5(d) is nearly dried out. SOH of the battery cycled for 2000 times degrades and a small amount of gas generates. Since the electrodes are on the left and right of the battery as Fig. 5(a) presents, the gas generated from the side reactions will gather around at the edge of the battery. But the cycling conditions demonstrate that it still behaves better than the faulty one, which also can be seen in the imaging results. A battery with the thickness of around 26 mm is imaged in Fig. S3, showing a great advancement of combining fiber optic sensor and ultrasound detection method for BHM.

The wetting process of AFLMB

For a commercial pouch cell, monitoring the wetting condition is of great importance in safe usage. When injecting a dry battery with the electrolyte, it will slowly flow into the cell until the battery is filled up. However, the insufficient wetting and uneven distribution will lead to lithium plating or other side reactions if the cycling starts under bad wetting quality. Hence, the experiment of using the proposed imaging system to monitor the wetting process of an AFLMB is carried out.

Figure 5(e) is the photograph of the AFLMB, which has a small size of 25 mm×18 mm×2.8 mm. The wetting process is monitored and presented in Fig. 5(f–h). Before filling the electrolyte, the central part of the battery is entirely blue, showing pretty low transmission of ultrasound wave. After injecting the electrolyte for 24 hours, the central part turns green as the edge part shows. When another 24 hours pass, the central part even transmits more ultrasound wave than the edge part. Therefore, the wetting process of a small battery like AFLMB could be less than 24 hours for commercial usage.

In Fig. 5(d) and Fig. 5(f), the images are both blue in the inner part, while the mechanisms can be very different. In Fig. 5(d), the gas in the battery greatly blocks and reflects the ultrasound, resulting in the low transmission. However, the reason that low transmission appears in Fig. 5(f) is the transmission path limitation. In the dry battery, the ultrasound only transmits in the solid particle with small number of paths, while in the "wetted" battery, the number of paths increases exponentially which allows more ultrasound to pass through.

The formation process of the AFLMB

After the AFLMB is entirely wetting with the electrolyte, the charging and discharging test is further carried out with a current of 30 mA. The blue curve in Fig. 6 shows
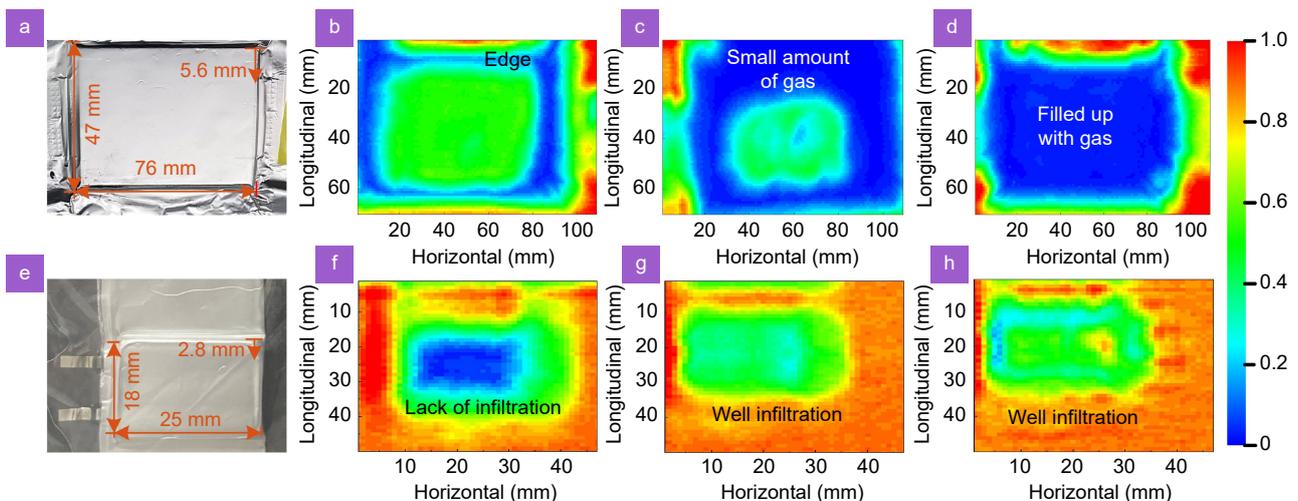

Fig. 5 | (**a**) Photograph of the LFP‖Gr battery. The ultrasound image of the (**b**) healthy battery, (**c**) battery cycled for 2000 times and (**d**) faulty battery. (**e**) The photo of the AFLMB. (**f**) The ultrasound image of the dry AFLMB. The ultrasound images of the AFLMB when it is injected with electrolyte after (**g**) 24 hours and (**h**) 48 hours.

the voltage variation during the test. During the charging process, the battery voltage rises rapidly to 3.75 V at the beginning. Then the voltage increases slowly until it reaches 4.3 V. While in the discharging process, the voltage decreases not too fast until it reaches 3.5 V. Meanwhile, the process is suspended once an hour for imaging, which results in the stagnation phenomenon in the voltage curve in Fig. 6. During the charging process, a sudden pause will reduce the voltage, while in the discharging process, it will lead to a voltage rise.
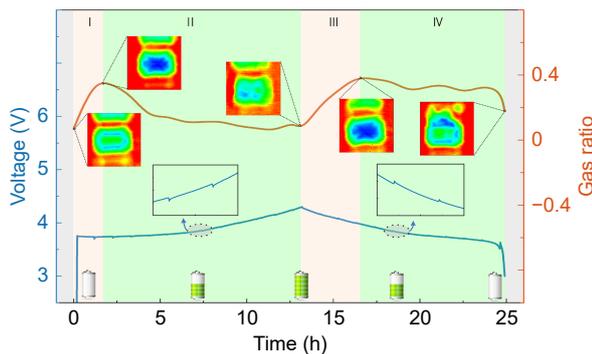

Fig. 6 | The galvanostatic curves and gas ratio variation of the pouch cell in the formation process.

The imaging results are analyzed and plotted as the red curve in Fig. 6. The gas ratio is obtained by dividing the gas area by the pouch cell area of every imaging result in Fig. S4 and Fig. S5, and the details are given in Fig. S6. As we can see that the gas generates at the beginning of the charging process and it almost fills up the battery. However, in the following process, the gas becomes unevenly distributed in the battery and gradually disappears. This is ascribed to the formation of the solid electrolyte interphase (SEI) in the first cycle. After the SEI basically forms in the charging process, gas generation reduces significantly. In the meantime, gas can flow into the gasbag above the battery. As a result, the gas amount reaches the peak before the charging process is finished.

While in the discharging process, gas continuously increases in the first four hours. Since the SEI is formed, the gas mainly comes from side reactions in the discharging process. In the following process, the accumulation of gas gradually reduces in the cell since some part of the gas escaped into the gasbag, which makes the signals of gasbag in the last picture at 25 h lower. Meanwhile, the gas is unevenly distributed in the gasbags. Hence, the proposed imaging system is capable of monitoring the internal changes during the formation process.

Conclusions

In summary, an ultrasound imaging system based on fiber optic ultrasound sensor is proposed and demonstrated for BHM. The proposed sensor tip owns the characteristics of miniaturization and compactness with a diameter of 4.5 mm, in which the high sensitivity of 558 mV/kPa and low NEP of 63.5 mPa at 500 kHz are experimentally demonstrated. Besides, the ultrasound sensitivity of the sensor is higher than 13.1 mV/kPa within the frequency range from 50 kHz to 1 MHz, with a bandwidth of 218 kHz. Based on the sensor tip, the imaging system exhibits a high resolution of 0.5 mm, which is suitable for the pouch cell monitoring. Furthermore, the safety monitoring of commercial LFP||Gr pouch cell is realized via this system, demonstrating that the SOH for different batteries can be clearly monitored and distinguished. Besides, the wetting and formation process of an AFLMB are monitored and the SEI growth is observed with an excellent performance. Therefore, the fiber optic ultrasound imaging system provides a novel approach for the BHM. In the future, with the sensor array and artificial intelligence adopted, the fast detection and intelligent recognition can be realized, which will further scall this technology for widespread commercial applications.

References

1. Marom R, Amalraj SF, Leifer N et al. A review of advanced and practical lithium battery materials. *J Mater Chem* **21**, 9938–9954 (2011).
2. Xiang JW, Yang LY, Yuan LX et al. Alkali-metal anodes: from lab to market. *Joule* **3**, 2334–2363 (2019).
3. Liu B, Zhang JG, Xu W. Advancing lithium metal batteries. *Joule* **2**, 833–845 (2018).
4. Li YP, Zhang Y, Li Z et al. Operando decoding of surface strain in anode-free lithium metal batteries via optical fiber sensor. *Adv Sci* **9**, 2203247 (2022).
5. Tarascon JM, Armand M. Issues and challenges facing rechargeable lithium batteries. *Nature* **414**, 359–367 (2001).
6. Lin XK, Khosravinia K, Hu XS et al. Lithium plating mechanism, detection, and mitigation in lithium-ion batteries. *Prog Energy Combust Sci* **87**, 100953 (2021).
7. Sun ZF, Li M, Xiao BS et al. In situ transmission electron microscopy for understanding materials and interfaces challenges in all-solid-state lithium batteries. *eTransportation* **14**, 100203 (2022).
8. Itou M, Orikasa Y, Gogyo Y et al. Compton scattering imaging of a working battery using synchrotron high-energy X-rays. *J Synchrotron Radiat* **22**, 161–164 (2015).
9. Chen HS, Yang SQ, Song WL et al. Quantificational 4D visualization and mechanism analysis of inhomogeneous electrolyte

wetting. *eTransportation* **16**, 100232 (2023).

10. Zinth V, von Lüders C, Hofmann M et al. Lithium plating in lithium-ion batteries at sub-ambient temperatures investigated by in situ neutron diffraction. *J Power Sources* **271**, 152–159 (2014).

11. Ziesche RF, Kardjilov N, Kockelmann W et al. Neutron imaging of lithium batteries. *Joule* **6**, 35–52 (2022).

12. Schindler S, Bauer M, Petzl M et al. Voltage relaxation and impedance spectroscopy as in-operando methods for the detection of lithium plating on graphitic anodes in commercial lithium-ion cells. *J Power Sources* **304**, 170–180 (2016).

13. Harlow JE, Glazier SL, Li J et al. Use of asymmetric average charge-and average discharge-voltages as an indicator of the onset of unwanted lithium deposition in lithium-ion cells. *J Electrochem Soc* **165**, A3595–A3601 (2018).

14. Robinson JB, Darr JA, Eastwood DS et al. Non-uniform temperature distribution in Li-ion batteries during discharge–a combined thermal imaging, X-ray micro-tomography and electrochemical impedance approach. *J Power Sources* **252**, 51–57 (2014).

15. Jiang BQ, Zhao JL. Nanomaterial-functionalized tilted fiber gratings for optical modulation and sensing. *J Lightwave Technol* **41**, 4103–4113 (2023).

16. Zheng HR, Liu Z, Li SC et al. Pd/WO_3 Co-deposited tilted fiber bragg grating for fast hydrogen sensing. *IEEE Trans Instrum Meas* **74**, 3522415 (2025).

17. Huang JQ, Albero Blanquer L, Bonefacino J et al. Operando decoding of chemical and thermal events in commercial Na(Li)-ion cells via optical sensors. *Nat Energy* **5**, 674–683 (2020).

18. Zhang Y, Li YP, Guo ZZ et al. Health monitoring by optical fiber sensing technology for rechargeable batteries. *eScience* **4**, 100174 (2024).

19. Zhang Y, Hao SP, Pei F et al. *Operando* chemo-mechanical evolution in $LiNi_{0.8}Co_{0.1}Mn_{0.1}O_2$ cathodes. *Natl Sci Rev* **11**, nwae254 (2024).

20. Matuck LC, Cabrita PD, Pinto JL et al. Customized optical fiber birefringent sensors to multipoint and simultaneous temperature and radial strain tracking of lithium‐ion batteries. *Adv Sens Res* **2**, 2200046 (2023).

21. Wang RL, Zhang HZ, Liu QY et al. *Operando* monitoring of ion activities in aqueous batteries with plasmonic fiber-optic sensors. *Nat Commun* **13**, 547 (2022).

22. Biazi V, Moreira AC, Pinto JL et al. A particle filter-based virtual sensor for estimating the state of charge and internal temperature of lithium-ion batteries: implementation in a simulated study case. *J Energy Storage* **61**, 106814 (2023).

23. Zhang SX, Li H, Fan CZ et al. Adaptive decentralized AI scheme for signal recognition of distributed sensor systems. *Opto-Electron Adv* **7**, 240119 (2024).

24. Davies G, Knehr KW, Van Tassell B et al. State of charge and state of health estimation using electrochemical acoustic time of flight analysis. *J Electrochem Soc* **164**, A2746–A2755 (2017).

25. Wu Y, Wang YR, Yung WKC et al. Ultrasonic health monitoring of lithium-ion batteries. *Electronics* **8**, 751 (2019).

26. Hsieh AG, Bhadra S, Hertzberg BJ et al. Electrochemical-acoustic time of flight: *in operando* correlation of physical dynamics with battery charge and health. *Energy Environ Sci* **8**, 1569–1577 (2015).

27. Deng Z, Huang ZY, Shen Y et al. Ultrasonic scanning to observe wetting and "unwetting" in li-ion pouch cells. *Joule* **4**, 2017–2029 (2020).

28. Yang LY, Li YP, Fang F et al. Highly sensitive and miniature microfiber-based ultrasound sensor for photoacoustic tomography. *Opto-Electron Adv* **5**, 200076 (2022).

29. Zhang L, Zhen YQ, Tong LM. Optical micro/nanofiber enabled tactile sensors and soft actuators: A review. *Opto-Electron Sci* **3**, 240005 (2024).

30. Shum PP, Keiser G, Humbert G et al. Highly sensitive microfiber ultrasound sensor for photoacoustic imaging. *Opto-Electron Adv* **6**, 230065 (2023).

31. Liu HH, Hu DJJ, Sun QZ et al. Specialty optical fibers for advanced sensing applications. *Opto-Electron Sci* **2**, 220025 (2023).

32. Chen G, Xia JJ. Non-contact shear wave generation and detection using high frequency air-coupled focused transducer and fiber optic based sagnac interferometer for mechanical characterization. *Sensors* **22**, 5824 (2022).

33. Wang JY, Ai F, Sun QZ et al. Diaphragm-based optical fiber sensor array for multipoint acoustic detection. *Opt Express* **26**, 25293–25304 (2018).

34. Yang LY, Xu DC, Chen G et al. Miniaturized fiber optic ultrasound sensor with multiplexing for photoacoustic imaging. *Photoacoustics* **28**, 100421 (2022).

35. Duque WS, Rodríguez Díaz CA, Leal-Junior AG et al. Fiber-optic hydrophone based on Michelson's interferometer with active stabilization for liquid volume measurement. *Sensors* **22**, 4404 (2022).

36. Li C, Lu SS, Zhong C et al. High-sensitivity low-frequency Fabry-Perot ultrasonic hydrophone with Chitosan diaphragm. *IEEE Sens J* **22**, 6669–6676 (2022).

37. Chen HB, Chen QQ, Wang W et al. Fiber-optic, extrinsic Fabry–Perot interferometric dual-cavity sensor interrogated by a dual-segment, low-coherence Fizeau interferometer for simultaneous measurements of pressure and temperature. *Opt Express* **27**, 38744–38758 (2019).

38. Yang LY, Dai CH, Wang AQ et al. Multi-channel parallel ultrasound detection based on a photothermal tunable fiber optic sensor array. *Opt Lett* **47**, 3700–3703 (2022).

39. Jiang JF, Zhang TH, Wang S et al. Noncontact ultrasonic detection in low-pressure carbon dioxide medium using high sensitivity fiber-optic Fabry–Perot sensor system. *J Lightwave Technol* **35**, 5079–5085 (2017).

40. Ma J, Xuan HF, Ho HL et al. Fiber-optic Fabry–Pérot acoustic sensor with multilayer graphene diaphragm. *IEEE Photonics Technol Lett* **25**, 932–935 (2013).

41. Feng DY, Zheng HR, Sun H et al. SnO_2/polyvinyl alcohol nanofibers wrapped tilted fiber grating for high-sensitive humidity sensing and fast human breath monitoring. *Sens Actuators B: Chem* **388**, 133807 (2023).

42. Guo YS, Jiang BQ, Liu L et al. In situ monitoring of curing reaction in solid composite propellant with fiber-optic sensors. *ACS Sens* **8**, 2664–2672 (2023).

Acknowledgements

Author contributions

Q. Z. Sun and G. Chen proposed the original idea. Q. Z. Sun supervised the project. G. Chen fabricated the sensors and demonstrated the imaging system. G. Chen and H. Li carried out the experiment. G. Chen, Y. Q. Liu, F. J. Zhang, and D. C. Xu. analyzed the data. G. Chen, H. Li, and Q. Z. Sun wrote the paper. Y. Zhang and Z. Li provided the AFLMB. A. Q. Wang, Z. Zhang, and Z. J. Yan participated the discuss of results, with all authors contributing to the discussion and preparation of the manuscript.

Competing interests

The authors declare no competing financial interests.